Diamond-Based Magnetic Imaging with Fourier Optical Processing

Mikael P. Backlund, Pauli Kehayias, and Ronald L. Walsworth*

Harvard-Smithsonian Center for Astrophysics, Cambridge, Massachusetts 02138, USA
and Department of Physics, Harvard University, Cambridge, Massachusetts 02138, USA

(Received 22 June 2017; published 3 November 2017)

Diamond-based magnetic field sensors have attracted great interest in recent years. In particular, wide-field magnetic imaging using nitrogen-vacancy (NV) centers in diamond has been previously demonstrated in condensed matter, biological, and paleomagnetic applications. Vector magnetic imaging with NV ensembles typically requires a significant applied field (> 10 G) to resolve the contributions from four crystallographic orientations, hindering studies of magnetic samples that require measurement in low or independently specified bias fields. Here we model and measure the complex amplitude distribution of NV emission at the microscope's Fourier plane and show that by modulating this collected light at the Fourier plane, one can decompose the NV ensemble magnetic resonance spectrum into its constituent orientations by purely optical means. This decomposition effectively extends the dynamic range at a given bias field and enables wide-field vector magnetic imaging at arbitrarily low bias fields, thus broadening potential applications of NV imaging and sensing. Our results demonstrate that NV-based microscopy stands to benefit greatly from Fourier optical approaches, which have already found widespread utility in other branches of microscopy.

DOI: 10.1103/PhysRevApplied.8.054003

I. INTRODUCTION

The unique properties of nitrogen-vacancy (NV) centers have made them powerful tools for micro- and nanoscale sensing over the past decade [1], and they are especially adept sensors of magnetic fields [2,3]. NV centers are C_{3v}-symmetric color centers of the diamond lattice formed by substitution of a nitrogen atom and a vacancy at neighboring lattice sites, as shown in Figs. 1(a)–1(c). Throughout this article, we refer to the negatively charged form of the NV center, which has an electronic spin-triplet ground state with a 2.87-GHz zero-field splitting between the $m_s = 0$ and $m_s = \pm 1$ magnetic sublevels as shown in Fig. 1(d), where the spin is quantized along the NV axis. A magnetic field $\mathbf{B}$ further splits these sublevels by the Zeeman effect. Illuminating a NV center with 532-nm laser light optically pumps it to the $m_s = 0$ sublevel, which luminesces more brightly than the $m_s = \pm 1$ sublevels. A resonant microwave field repopulates the $m_s = \pm 1$ sublevels and reduces the photoluminescence (PL) intensity. Measuring PL as a function of microwave frequency yields an optically detected magnetic resonance (ODMR) spectrum, from which one can calculate $\mathbf{B}$ by precisely measuring the Zeeman shifts of the spin sublevels.

A dense ensemble of NV centers in a layer near the surface of a diamond chip can be used to simultaneously measure the magnetic field at each point along the surface and so comprises a wide-field magnetic imaging device. Such an imaging platform has been utilized previously across a diverse set of applications, including studies pertaining to condensed matter physics [4], cell biology [5,6], and paleomagnetism [7,8]. In a NV ensemble, there are typically equal populations of the four possible NV orientations within the diamond crystal, with spin-quantization axes parallel to $\{\hat{\mathbf{u}}_1, \hat{\mathbf{u}}_2, \hat{\mathbf{u}}_3, \hat{\mathbf{u}}_4\}$ as illustrated in Figs. 1(a) and 1(b). In Fig. 1 and throughout this study, we treat the case in which the sensing surface is perpendicular to the [001] axis of the diamond crystal, and the optical axis of the microscope is along the [001] axis. In this common configuration, the four NV orientations are treated symmetrically. Since $\mathbf{B}$, in general, will have a different projection on each $\hat{\mathbf{u}}_j$, resonances due to each of the four orientations will shift differently. As a result, the ODMR spectrum contains eight major lines (four orientations times two spin transitions). Measuring the projection of $\mathbf{B}$ onto each NV axis allows one to compute the vector components of the field. Hyperfine interaction with the ^{14}N nucleus further splits (by 2.16 MHz) each of the eight major lines into triplets [9], though this fact is tangential to the main focus of this study.

If the resonances due to different NV orientations overlap with one another, ambiguity in the extracted magnetic field can arise. To avoid this issue, a sufficiently strong bias field $\mathbf{B}^{(\mathrm{bias})}$ is typically applied to deliberately separate the peaks by frequency spacings that are significantly larger than the shifts expected from the field of the sample. However, a strong applied field is undesirable for many applications, including paleomagnetic studies of geological and meteorite samples in which an induced signal from paramagnetic and low-coercivity grains may overwhelm the

*rwalsworth@cfa.harvard.edu

 © 2017 American Physical Society

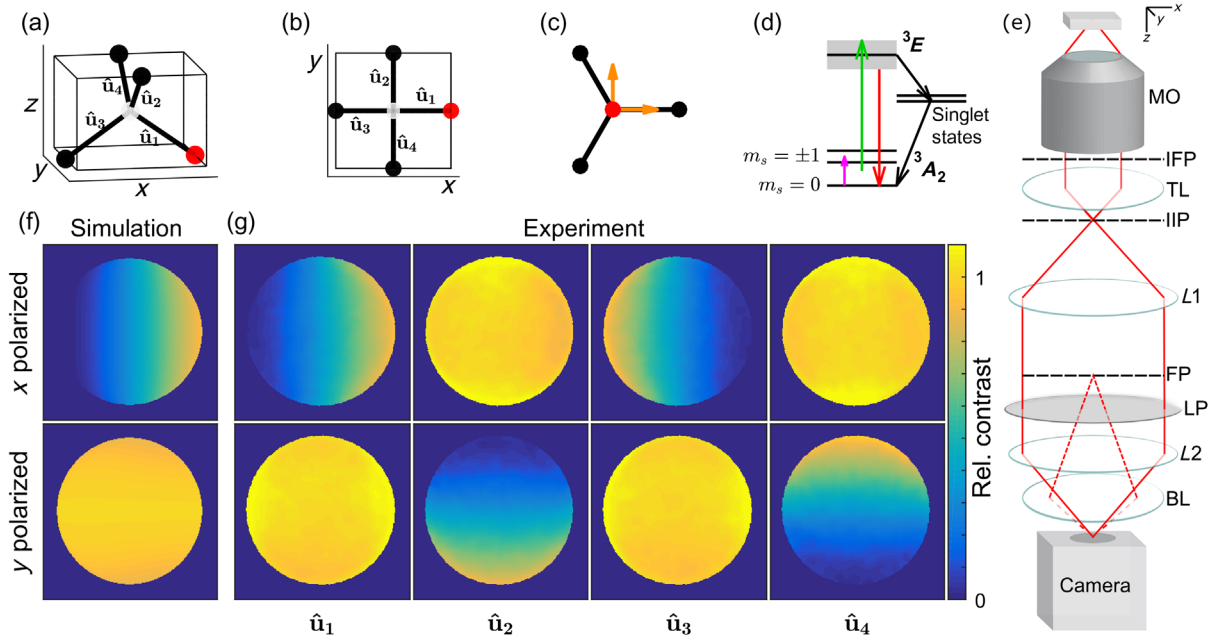


FIG. 1. Setup and Fourier-plane patterns of NV ensemble photoluminescence. (a) Sketch of NV center pointing along $\hat{\mathbf{u}}_1$, including three carbon atoms (black spheres), nitrogen atom (red), and vacancy (gray). Lines parallel to each NV orientation class $\hat{\mathbf{u}}_j$ are labeled. Facets of the illustrated rectangular prism coincide with those of the diamond samples used in our experiments and are perpendicular to the [110], $[1\bar{1}0]$, and [001] crystal axes. (b) xy perspective of lattice shown in (a). (c) View of NV along its axis, with transition electric dipole moments (orange). (d) Simplified NV energy-level diagram (level spacings not to scale). The electronic $^3A_2$ ground state consists of $m_s = 0$ and $m_s = \pm 1$ magnetic sublevels split by $D = 2.87$ GHz. The Zeeman effect further splits $m_s = \pm 1$ in response to a magnetic field. Applied microwaves (magenta) facilitate transitions from $m_s = 0$ to $m_s = \pm 1$. A 532-nm laser is applied to drive optical transitions to the ^3E manifold. Red PL is collected upon radiative relaxation to the ground state. Nonradiative relaxation through the singlet-state channel is responsible for the spin-state-dependent PL contrast and initialization into $m_s = 0$. (e) Schematic of optical setup, tracing collected PL from the diamond chip to the camera: microscope objective (MO), intermediate Fourier-plane (IFP), tube lens (TL), intermediate image plane (IIP), $4f$ lens ($L1$), Fourier plane (FP), linear polarizer (LP), and either $4f$ lens ($L2$) or Bertrand lens (BL) depending on whether the measurement calls for imaging real or Fourier space. (f) Simulation of PL contrast distribution in the Fourier plane for a NV oriented along $\hat{\mathbf{u}}_1$ with a NA = 1.49 oil objective. (g) Experimentally measured NV ensemble PL contrast distributions in the Fourier plane due to each NV orientation.

ferromagnetic signal of interest [8,10]. In other applications, it may be necessary to reserve the applied field for another function, e.g., for controlling magnetic nanoparticles within a cell [11] or tuning the properties of a magnetic material [12,13]. A method to resolve contributions of each NV orientation to the ODMR spectrum that does not rely on an applied magnetic field is, thus, desirable. Here we present such a method based on Fourier-plane processing [14], relying only on downstream optical components to achieve the desired decomposition.

II. RESULTS AND DISCUSSION

A. Fourier-plane signatures of NV emission

The method we present exploits the selection rules of the NV center's $^3E \rightarrow {}^3A_2$ optical transition illustrated in Fig. 1(d) [15–17]. At room temperature, this transition can be considered to proceed via two mutually incoherent, orthogonal transition electric dipoles oriented perpendicular to the NV axis, as shown in Fig. 1(c). In the paraxial regime (valid downstream of the objective), optical polarization alone cannot distinguish emission between orientation pairs $\hat{\mathbf{u}}_j$ and $\hat{\mathbf{u}}_{j+2}$, as symmetry of the transition dipoles dictates that the x-polarized (y-polarized) emission due to both will have equal total intensities. To gain deeper insight, we simulate NV PL for each of the four orientations by adapting previous work modeling electric dipole emission near interfaces (see Appendix A for more details) [18–23]. Our simulations predict a characteristic distribution of PL intensity and contrast (i.e., PL intensity on resonance divided by PL intensity off resonance) for each orientation at the microscope's Fourier plane, as depicted in Fig. 1(f) for the example of $\hat{\mathbf{u}}_1$ NVs. Further pictorial explanation of these patterns is given in Fig. S1 of the Supplemental Material [24]. Briefly, for each orientation, we can consider one transition dipole lying in the plane perpendicular to the optical axis and the other transition dipole with a significant component out of this plane. Take, for example, a NV oriented along $\hat{\mathbf{u}}_1 = [\sqrt{2/3}, 0, -1/\sqrt{3}]^T$, as defined relative to the lab frame coordinates depicted in Fig. 1(a). The out-of-plane dipole points along

$[-1/\sqrt{3}, 0 - \sqrt{2/3},]^T$ and emits light that when viewed along the optical axis in the far field is mostly polarized along x. Because of the characteristic anisotropic dipole emission pattern, the light due to this out-of-plane dipole illuminates the Fourier plane with a spatial gradient along x, as seen in the top panel of Fig. 1(f). On the other hand, the in-plane transition electric dipole of a NV oriented along $\hat{\mathbf{u}}_1$ lies along $[0, 1, 0]^T$ and emits mostly y-polarized light. Its orientation relative to the optical axis renders a more uniform distribution of light at the Fourier plane, as seen in the bottom panel of Fig. 1(f). The Fourier-plane patterns due to NVs oriented along $\hat{\mathbf{u}}_2$, $\hat{\mathbf{u}}_3$, and $\hat{\mathbf{u}}_4$ are obtained by simple symmetry operations on those due to $\hat{\mathbf{u}}_1$ NVs.

To experimentally confirm these simulated Fourier-plane patterns, we employ the setup sketched in Fig. 1(e), using a Bertrand lens to relay the Fourier plane onto the camera and a linear polarizer inserted into the collection path to pass either x- or y-polarized PL. We measure the Fourier-plane distribution of ODMR contrast due to each NV orientation by first applying a sufficiently strong $\mathbf{B}^{(\mathrm{bias})}$ to resolve the ODMR lines of each orientation, then integrating the PL decrease under each isolated microwave resonance peak. Following this procedure while imaging the Fourier plane directly gives the spatial contrast maps shown in Fig. 1(g), indicating excellent agreement between simulation and experiment. We next seek to leverage this effect to decompose the ODMR for general $\mathbf{B}^{(\mathrm{bias})}$.

B. Fourier optical decomposition of ODMR spectrum

Fourier optical decomposition of the ODMR spectrum is achieved by making four sequential measurements, as depicted schematically in Fig. 2(a). We define $\tilde{c}_1(f)$ as the NV ensemble ODMR spectrum recorded with an x-oriented linear polarizer in the emission path and the left half of the pupil blocked. (Throughout this paper, we use the term "pupil" interchangeably with "Fourier plane.") We define $\tilde{c}_2(f)$, $\tilde{c}_3(f)$, and $\tilde{c}_4(f)$ similarly [refer to Fig. 2(a)]. Together, these four measurements comprise the measurement array $\tilde{\mathbf{C}} \in \mathbb{R}^{4\times N_f}$, where N_f is the number of microwave frequencies sampled. Note that $\langle \tilde{c}_i(f) \rangle = \frac{1}{4}\sum_i \tilde{c}_i(f)$ represents a conventional ODMR spectral measurement without filtering, as exemplified in Figs. 2(b) and 2(c). In Fig. 2, we present two data sets, one in which $\mathbf{B}^{(\mathrm{bias})}$ resolves the resonances of each orientation [Figs. 2(b), 2(d), and 2(f)] and one in which it does not [Figs. 2(c), 2(e), and 2(g)]. We define Δ_B as

$$\Delta_B = \max |\mathbf{B}^{(\mathrm{bias})} \cdot \hat{\mathbf{u}}_j| - \min |\mathbf{B}^{(\mathrm{bias})} \cdot \hat{\mathbf{u}}_{j'}| \qquad (1)$$

enumerating the range in projections of the bias field onto the set of NV orientations and, in turn, the degree of overlap of the resonances. For data in Figs. 2(b), 2(d), and 2(f), $\Delta_B = 19.52$ G, while $\Delta_B = 0.42$ G for the data in Figs. 2(c), 2(e), and 2(g). The latter value is not a

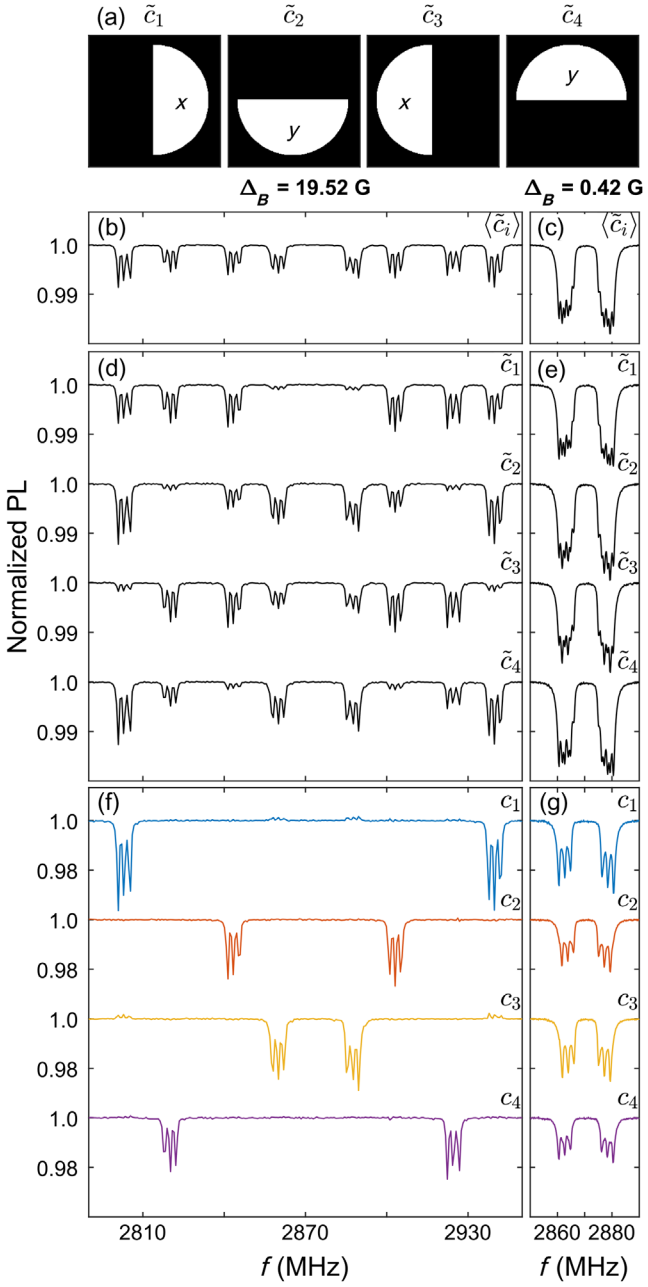


FIG. 2. Fourier decomposition of optically detected magnetic resonance spectrum. (a) Schematic depicting the passed polarization as well as the integrated or discarded portions of the pupil for measurement of each spectrum $\tilde{c}_i(f)$. (b) Conventional NV ensemble ODMR spectrum realized by computing the average of four measurements $\langle \tilde{c}_i(f) \rangle$ at high $\Delta_B (= 19.52$ G) such that eight resonances are clearly resolved. Each resonance appears as a triplet due to approximately 2.16-MHz splitting from the ^{14}N hyperfine interaction. (c) Same as (b) but at low $\Delta_B (= 0.42$ G) such that resonances from different NV orientations are not resolved. (d) ODMR measured under each of the four conditions sketched in (a) at $\Delta_B = 19.52$ G. (e) Same as (d) but instead at $\Delta_B = 0.42$ G. (f) Resulting ODMR spectra after Fourier decomposition at $\Delta_B = 19.52$ G. (g) Same as (f) but instead at $\Delta_B = 0.42$ G. The highly overlapping ODMR peaks obscure the hyperfine splittings in (c) and (e), whereas (g) shows that they are clearly revealed by the transformation. Different spectra within the same panel in (d)–(g) are offset for clarity.

fundamental minimum for Δ_B and is chosen only qualitatively during the experiment to visually overlap the ODMR peaks. Throughout our studies, we apply a bias field such that $\min|\mathbf{B}^{(\mathrm{bias})}\cdot\hat{\mathbf{u}}_j| > 1.4$ G in order to simplify our analysis and focus on the technological advancement at hand. At lower $\min|\mathbf{B}^{(\mathrm{bias})}\cdot\hat{\mathbf{u}}_j|$, ODMR spectra become complicated by level crossings as the Zeeman splitting approaches splittings due to crystal strain and the ^{14}N hyperfine interaction [9]. The latter issue can be addressed by ^{15}N enrichment and controlled circular microwave polarization [25–27], which is compatible with our all-optical technique. We reserve the technical work of combining these methods for future studies, which should ultimately enable vector magnetic sensing well below $\min|\mathbf{B}^{(\mathrm{bias})}\cdot\hat{\mathbf{u}}_j| = 1.4$ G. We further note that the ability to operate at the minimum bias fields explicitly demonstrated in the current study is nonetheless significant since, for instance, natural magnetite grains have coercivities in the range of approximately 2–20 G [28].

We first demonstrate our method by directly imaging the Fourier plane, taking sequential ODMR measurements of different polarizations, and integrating halves of the pupil plane in postprocessing. Individual $\tilde{c}_i(f)$ measurements are shown in Figs. 2(d) and 2(e) for high and low Δ_B, respectively. From simulation, we expect that for each measurement configuration $\tilde{c}_i$, the resonances due to each of the four orientations should have relative weights $w_1 = 0.226$, $w_2 = 0.363$, $w_3 = 0.049$, and $w_4 = w_2$. The average experimentally measured weights are $w_1 = 0.220(4)$, $w_2 = 0.360(7)$, and $w_3 = 0.060(2)$. Note that the values of these weights depend on the NA of the objective. The values reported above are valid for a NA 1.49/oil immersion objective, consistent with the experimental data reported here thus far. The imaging experiments described in the following section instead employ a NA 0.75/air immersion objective and so obviously require the weighting values corresponding to these parameters to properly process the data (see Appendix C).

We define $\mathbf{C} \in \mathbb{R}^{4\times N_f}$ containing the underlying ODMR spectrum $c_j(f)$ for each NV orientation, yielding

$$\tilde{\mathbf{C}} = \mathbf{W}\mathbf{C}, \tag{2}$$

where $\mathbf{W}$ is the circulant matrix [29] formed by permuting $[w_1, w_2, w_3, w_2]$:

$$\mathbf{W} = \begin{pmatrix} w_1 & w_2 & w_3 & w_2 \\ w_2 & w_1 & w_2 & w_3 \\ w_3 & w_2 & w_1 & w_2 \\ w_2 & w_3 & w_2 & w_1 \end{pmatrix}. \tag{3}$$

In practice, we do not enforce the symmetry of Eq. (3) and instead measure each element of $\mathbf{W}$ individually to better compensate for experimental nonidealities (see Appendix C). The underlying isolated ODMR spectrum of each individual orientation can be estimated as

$$\hat{\mathbf{C}} = \mathbf{W}^{-1}\tilde{\mathbf{C}}. \tag{4}$$

The high-Δ_B demonstration in Fig. 2(f) proves the capability of isolating the ODMR features of the individual NV orientations. From Fig. 2(f), we can quantify an average cross-talk error of approximately 1%, as determined by comparing the absolute value of the integral under each would-be nulled resonance to the non-nulled resonance. Figure 2(g) demonstrates this newfound capability in the more useful low-Δ_B regime.

C. Vector magnetic imaging at low bias fields

To demonstrate wide-field imaging with Fourier-plane modulation, we remove the Bertrand lens and add the lens $L2$ [Fig. 1(e)]. The lenses $L1$ and $L2$ form a $4f$ optical processing unit [14], a commonly used optical correlator so named because of the total length it occupies: one focal length from the intermediate image plane to $L1$, plus a focal length to the Fourier plane, plus a focal length to $L2$, plus a fourth focal length to the final image. At the Fourier plane formed between $L1$ and $L2$, we place a knife-edge beam block to alternately obscure halves of the pupil. While the beam block modifies the microscope's point-spread function (PSF) (see Fig. S2 in Ref. [24]), an image is, nonetheless, relayed to the camera, and the measurement procedure yields the ODMR spectrum $\tilde{c}_i(x_k, y_k, f)$ in each pixel k. After pixelwise transformation via Eq. (4), each isolated $c_j(x_k, y_k, f)$ spectrum is fit, and the vector magnetic field is reconstructed across the image. We apply this procedure to image the field from a ferromagnetic bead placed directly on the surface of a diamond containing a 3.8-μm NV layer (Fig. 3; additional beads in Fig. S3 of Ref. [24]). To establish a ground truth, we first resolve the resonances of each orientation [Fig. 3(a)] at high Δ_B and infer the sample field [Figs. 3(b)–3(d)] in the conventional way [10]. Next, we reduce Δ_B to overlap the resonances [Fig. 3(e)]. Using our method, we decompose the unresolved spectrum and infer the vector magnetic field image [Figs. 3(f)–3(i)]. Comparable fits to magnetic dipole sources are shown in the insets of Figs. 3(b)–3(d) and 3(f)–3(h). At high Δ_B, we estimate the following parameters for the dipolar source from a nonlinear least-squares fit: x position $= -0.2(1)$ μm, y position $= -0.3(1)$ μm, standoff distance $= 8.9(1)$ μm, magnetic dipole moment $= 29(1)\times10^{-15}$ J/T, azimuthal orientation $= 82(1)°$, and polar orientation $= 110(1)°$. At low Δ_B, we find these estimates: x position $= -0.6(1)\,\mu$m, y position $= -0.3(1)\,\mu$m, standoff distance $= 8.7(2)\,\mu$m, magnetic dipole moment $= 26(1)\times10^{-15}$ J/T, azimuthal orientation $= 82(1)°$, and polar orientation $= 112(1)°$. The fit parameter errors are an average 95% confidence intervals determined using the MATLAB function `nparci`. Note that the discrepancy

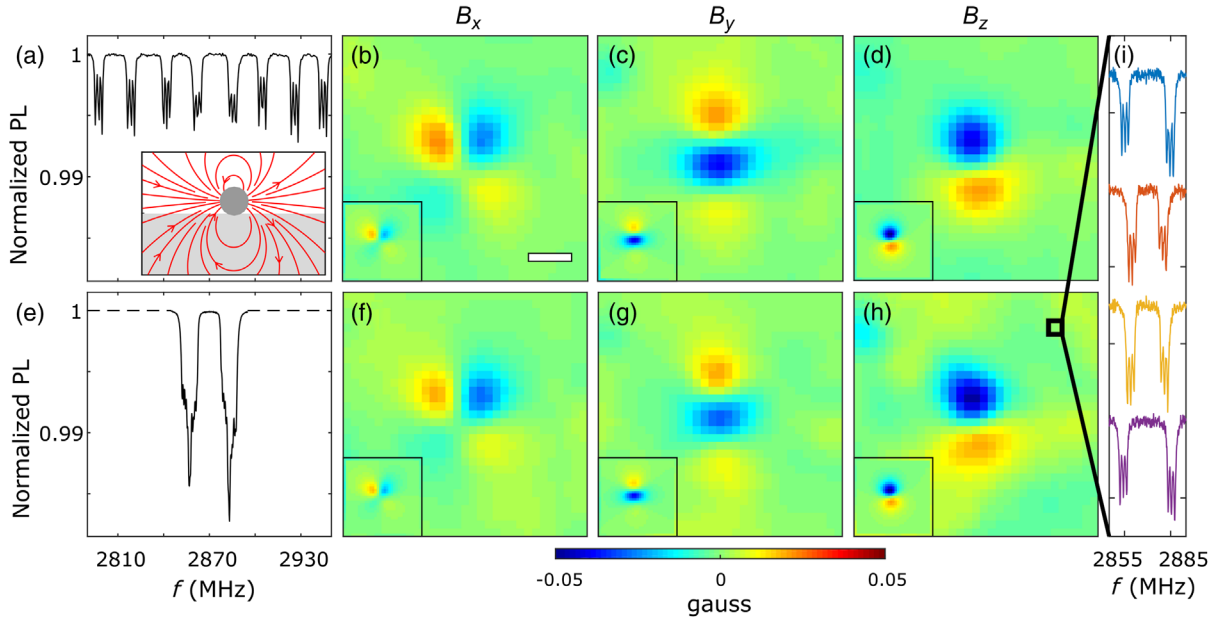


FIG. 3. Magnetic bead imaging with Fourier optical decomposition. (a) Spatially averaged NV ensemble ODMR spectrum at $\Delta_B = 22.16$ G such that resonances are well resolved. Inset: illustration of magnetic bead on diamond surface with magnetic field lines (red). (b)–(d) images of x, y, and z components of magnetic field due to a magnetic bead determined at $\Delta_B = 22.16$ G without optical decomposition. Insets show calculated field components from least-squares fit to magnetic dipole source. Scale bar: 10 μm. (e) Spatially averaged NV ensemble ODMR spectrum from measurement at $\Delta_B = 1.99$ G such that resonances are not resolved. (f)–(h) Images of x, y, and z components of stray magnetic field due to the same magnetic bead as in (b)–(d) but determined at $\Delta_B = 1.99$ G with Fourier optical decomposition. Insets show calculated field components from least-squares fit to magnetic dipole source. (i) Decomposed ODMR spectra of an arbitrary pixel of the low-Δ_B measurement showing estimated $c_1(f)$ (blue), $c_2(f)$ (orange), $c_3(f)$ (yellow), and $c_4(f)$ (purple), offset for clarity.

in the estimated lateral position may be largely due to the drift and registration error of the sequentially recorded images.

This demonstration shows that the Fourier optical decomposition method can be used to accurately reconstruct vector magnetic images at low applied fields for which overlapping resonances will otherwise lead to ambiguity. We emphasize here that the utility of our method is in overcoming such ambiguities in cases where the bias field is otherwise constrained. Our method does not improve magnetic field *sensitivity* relative to the usual method of applying a strong bias field and, in fact, yields reduced sensitivity (see Fig. S4 and accompanying text in the Supplemental Material [24]), in part due to the sequential nature of the present measurement. In future implementations, some of this difference can be recovered by parallelizing the measurement by splitting the collected light with the appropriate beam splitters and detecting the four channels simultaneously. However, even the parallel Fourier optical decomposition measurement will impose a reduced sensitivity relative to the typical high-Δ_B measurement. This sensitivity penalty is lessened with increasing NA (see Fig. S4 and Supplemental Material [24]).

A nice feature of Fourier optical decomposition is that it greatly extends the accessible dynamic range at a given bias field. A sample may be able to withstand a modest applied field such that the resonances of each NV orientation are resolved throughout much of the imaging area, but ambiguities will still arise in regions where the local sample field is comparable to the applied field. Such ambiguities can result in local field reconstruction failures. To demonstrate how Fourier optical decomposition can circumvent this limitation, we image a 30-μm-thin section of the Allende CV3 chondrite, a widely studied meteorite thought to be magnetized by a possible dynamo of its parent planetesimal [10,30]. For this proof-of-principle measurement, we expedite our search for strong local features by imparting a strong magnetization through the application of a 2000-G isothermal remanent magnetization (IRM) [31] field to the sample before imaging. During the measurement, an external bias field with $\Delta_B = 8.42$ G is applied in order to just resolve the NV ODMR peaks in the absence of the sample's field (see Fig. S5 in Ref. [24]). The ODMR peaks shift and overlap considerably in some regions, collapsing into two or four broad peaks and leading to ambiguities in the field components when treated without decomposition. While sample field reconstruction fails with the conventional technique (see Fig. S5 in Ref. [24]), our Fourier decomposition technique allows us to determine the vector magnetic images shown in Figs. 4(a)–4(c). The pattern revealed in Figs. 4(a)–4(c) resembles the field due to two strong dipolar features atop a slowly varying background

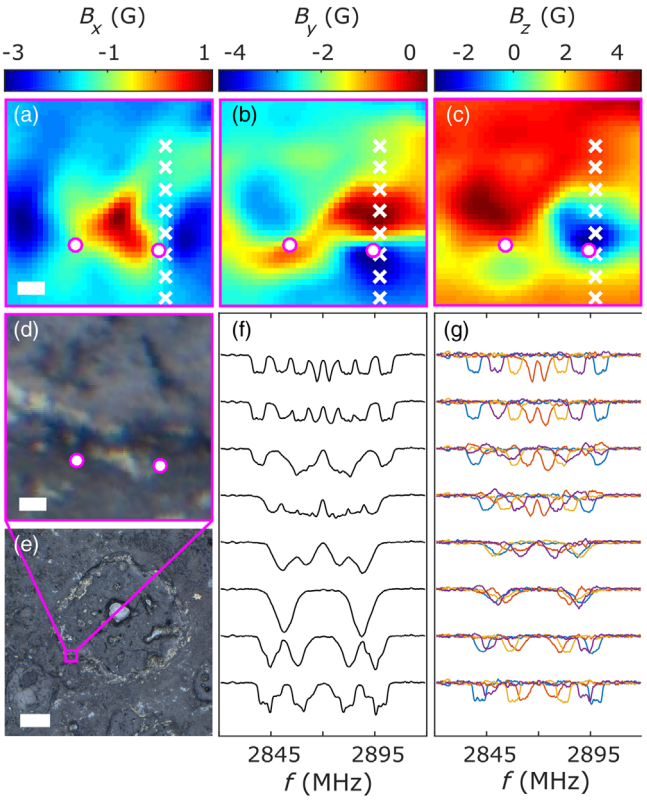


FIG. 4. Meteorite magnetic imaging with Fourier optical decomposition. (a)–(c) Images of x, y, and z components of the magnetic field due to a subregion of the Allende meteorite sample, as determined using Fourier optical decomposition to resolve ambiguities from overlapping ODMR peaks. $\Delta_B = 8.42$ G. Scale bar: 25 μm. (d) Reflection bright-field image of same region of the meteorite as in (a)–(c). Scale bar: 25 μm. (e) Reflection bright-field image showing larger field of view around the region imaged in (a)–(d) indicated by the magenta square. Scale bar: 500 μm. In each of (a)–(d), the fit xy positions of two magnetic dipole sources are marked with magenta circles (see Fig. S6 in Ref. [24]). (f) Example ODMR spectra without Fourier decomposition in the pixels marked with "x" in (a)–(c). The eight resonances collapse into two or four features in some pixels, resulting in ambiguity. (g) Fourier optical decomposition applied to the same ODMR spectra as in (f) showing individual contributions due to only $c_1(f)$ (blue), $c_2(f)$ (orange), $c_3(f)$ (yellow), and $c_4(f)$ (purple). Hyperfine features in (f) and (g) are blurred due to a combination of strong spatial gradients of the sample and a boxcar filter applied to improve the SNR (see Appendix C). Spectra within the same panel in (f) and (g) are offset for clarity.

(see Fig. S6 in Ref. [24] for the least-squares fit to this model), where the fitted xy positions of the two dipoles are marked in Fig. 4 by magenta circles. The dipole on the left has best-fit azimuthal orientation $-103(3)°$ and polar orientation 87(3)°; the dipole on the right has best-fit azimuthal orientation 106(4)° and polar orientation 137 (3)°. Figures 4(d) and 4(e) show a bright-field image that maps the positions of these two dipolelike sources to the edge of a chondrule, the main circular structure of diameter approximately 2 mm visible in whole in Fig. 4(e). Here, Fig. 4(d) corresponds to the same field of view as in Figs. 4(a)–4(c), and Fig. 4(e) shows a zoomed-out region containing this field of view. Figures 4(f) and 4(g) give further insight, displaying the ODMR spectra with and without decomposition along a slice of the image. Our method effectively increases the dynamic range in this measurement by at least a factor of 3 (see Fig. S5 in Ref. [24]) without the need to increase $|\mathbf{B}^{(\mathrm{bias})}|$.

III. CONCLUSION

In conclusion, we demonstrate a Fourier optical decomposition method to realize NV ensemble vector magnetic imaging without the need of a large bias magnetic field to resolve the contributions from each NV orientation. This method enables vector magnetic imaging in applications where a large bias field may induce unwanted magnetization of the sample or is otherwise constrained by other experimental parameters. As we show, Fourier optical decomposition effectively increases the dynamic range of the magnetic measurement at any particular applied field. Since it relies only on manipulation of downstream optics, the technique is compatible with most standard NV imaging apparatuses, including both wide-field and point detection (e.g., confocal scanning) geometries. (At the Fourier plane, the optical field due to emission from an on- or off-axis source is distinguished only by a linear phase factor, and so the amplitude-modulation scheme presented here is shift invariant.) Furthermore, since it requires simple and inexpensive components to implement, its appeal should be broad. For these reasons, Fourier optical decomposition has the potential to significantly increase the applicability of NV sensing and imaging technologies. Our simulations and experimental data uncover a wealth of information at the Fourier plane of a NV microscope. As Fourier optical techniques have found widespread utility in other realms of optical imaging [14,18,32,33], it is likely that similar approaches will enable future developments in NV-based platforms.

ACKNOWLEDGMENTS

This material is based upon work supported by, or in part by, the United States Army Research Laboratory and the United States Army Research Office under Grant No. W911NF1510548, as well as by the National Science Foundation Electronics, Photonics and Magnetic Devices (EPMD); Physics of Living Systems (PoLS); and Integrated NSF Support Promoting Interdisciplinary Research and Education (INSPIRE) programs. P. K. acknowledges support from the Intelligence Community Postdoctoral Research Fellowship Program. We thank Benjamin Weiss for the Allende sample and for use of his reflection microscope, Eduardo Lima for help with bright-field reflection microscopy, and Roger Fu for applying the IRM on the Allende sample and for helpful

discussions. We also thank David Glenn, Mark Ku, John Barry, Jennifer Schloss, and Matthew Turner for helpful discussions.

M. P. B. did the calculations and analysis. M. P. B. and P. K. did the experiments. M. P. B., P. K., and R. L. W. reviewed all the results and wrote the paper. R. L. W. supervised the project.

Note added.—Recently, we became aware of an alternative approach to NV ODMR decomposition that simultaneously exploits optical and microwave absorption selection rules for NV ensemble vector magnetometry [34]. We reiterate that at very low applied sample fields (<100 mG) microwave polarization control typically must be reserved to distinguish transitions to $m_s = \pm 1$, and so our all-optical method is compatible with such conditions.

APPENDIX A: OPTICAL SIMULATION

We simulate NV emission by adapting existing code [32], in turn, based on earlier works [18–20,22,23] modeling electric dipole emission near interfaces and collected with a high-NA objective. For the present work, we model a NV of a given orientation as two mutually incoherent radiating electric dipoles oriented perpendicular to the NV axis as sketched in Fig. 1(c). We approximate the emission to be monochromatic with wavelength 700 nm, near the peak of the NV^- emission spectrum at room temperature [1]. Briefly, we compute the complex-valued electric field at the Fourier plane of the microscope by decomposing into constituent plane waves, each carrying a complex amplitude according to the emitter's orientation and defocus, as well as the appropriate Fresnel coefficients incurred as a result of transmission through the diamond-immersion medium interface. When modeling the detection of NVs located at the far surface of the diamond, we also include Fresnel coefficients describing reflection from the far diamond-air interface. We perform simulations for both a NA 1.49 oil-immersion objective and a NA 0.75 air-immersion objective, as both are used in our experiments. To approximate the two diamond samples used in our experiments, we simulate a NV ensemble containing equal populations of each of the four orientations distributed uniformly throughout a surface layer with depth of either $d = 3.8$ or 0.9 μm (corresponding to samples $D1$ and $D2$ described below, respectively), with NV depth sampled every 10–100 nm. To match experimental conditions, the high-NA simulation of Fig. 1(f) places the NV layer at the (near) diamond-oil interface, while the low-NA simulation of Fig. S7 in Ref. [24] places the NV layer at the (far) diamond-air interface. The PSF shown in Fig. S2 in Ref. [24] is computed by taking the Fourier transform of the Fourier-plane complex amplitude, then taking the square modulus. As is true in our imaging experiments, we assume a magnification of 30× and a camera pixel size of 5.5 μm (183.3-nm pixels projected back to the object plane). The blocked and polarized PSF in Fig. S2 of Ref. [24] is computed by constraining support in the pupil plane to only x-polarized light in the right half of the Fourier disk then taking the Fourier transform to propagate to the image plane.

APPENDIX B: EXPERIMENTAL METHODS

We use two diamond samples (made by Element Six), each grown by chemical vapor deposition. Sample $D1$ contains a surface NV layer of thickness 3.8 μm (as determined by secondary ion mass spectroscopy) and nitrogen concentration of approximately 21 ppm. Sample $D2$ contains a surface NV layer of thickness 0.9 μm and nitrogen concentration of approximately 7 ppm. Both diamond chips have dimensions $4 \times 4 \times 0.5$ mm^3.

NVs are excited in a wide-field epi-illumination geometry, with 532-nm laser light coupled continuously into the back aperture of the objective via a dichroic mirror (Di02-R635, Semrock). The laser is linearly polarized along the axis $[1/\sqrt{2}, 1/\sqrt{2}, 0]^T$ (refer to the lab frame coordinates in Fig. 1) such that each NV orientation is excited at equal rates. At the NV layer, the laser beam peak intensity range is approximately 7–360 W/cm^2. NV PL is collected with one of two objectives: (1) NA 1.49/oil (CFI Apo TIRF 100x, Nikon) or (2) NA 0.75/air (CFI Plan Apo VC 20x, Nikon). Collected PL then is transmitted back through the aforementioned dichroic and relayed to the camera by several mirrors and the train of lenses sketched in Fig. 1(e). The tube lens TL ($f_{\mathrm{TL}} = 300$ mm) is placed a distance f_{TL} from the back aperture of the objective, and then the first $4f$ lens $L1$ ($f_{L1} = 200$ mm) is placed a distance $f_{\mathrm{TL}} + f_{L1}$ from the tube lens. The Fourier plane (FP) is formed a distance f_{L1} behind lens $L1$. To perform Fourier optical decomposition on the ODMR spectrum across an image, we place an opaque knife edge mounted on a rotation mount at this FP. For imaging experiments, a second $4f$ lens $L2$ ($f_{L2} = 200$ mm) is then placed a distance f_{L2} behind the FP, forming an image on the camera (acA2040–180 km, Basler) a distance f_{L2} behind $L2$. To image the Fourier plane directly as in Fig. 1(g), we remove $L2$ and place a Bertrand lens BL ($f_{\mathrm{BL}} = 75$ mm) at a distance of approximately 300 mm from the FP. This distance is determined first roughly using the thin-lens equation, then fine-tuned to focus the FP at a common objective height as for the image. The linear polarizer is placed just before the BL, though its precise placement is not important since the optical train behind the objective is well within the paraxial regime. A band-pass filter (BrightLine Fluorescence Filter 726/128, Semrock) is placed on the outer aperture of the camera.

For the direct measurements of the Fourier plane depicted in Figs. 1 and 2, we use the NA 1.49 oil-immersion objective. The diamond $D1$ is oriented such that the NV layer is on the side facing the objective, directly

in contact with the immersion oil. For the imaging experiments depicted in Figs. 3 and 4, this geometry cannot be used since the magnetic sample has to be placed in close proximity to the NV layer. Thus, the diamond ($D1$ for magnetic bead measurements, $D2$ for the Allende study) is flipped over, and the objective is focused through the bulk diamond. Imaging through the high-index ($n = 2.417$) diamond has a significant effect on the microscope's PSF (see Fig. S2 in Ref. [24]). Because of its short working distance, the NA 1.49 objective cannot be used to image through the diamond (thickness of approximately 0.5 mm), and so imaging experiments are done instead with the NA 0.75/air objective. Future implementations can be done with a thinned diamond chip such that a high-NA objective can still be used, as the sensitivity of the ODMR decomposition improves with increasing NA (see Fig. S4 in Ref. [24]).

The external magnetic bias field is applied with a neodymium magnet mounted above the diamond. Microwaves are supplied with a TPI-1001-B synthesizer (Trinity Power, Inc.) and amplified with a ZHL-16W-43+ amplifier (Mini-Circuits), outputting approximately 16 W of microwave power. Microwaves are delivered to the diamond via a copper wire loop oriented such that the microwave magnetic field has roughly equal projection on all four NV axes. The camera (operating with 5-ms exposure times) and microwave synthesizer are controlled with custom LabView and MATLAB software. Microwave power is toggled on and off in alternating images to help mitigate noticeable intensity drift from the laser. In each experiment, we sample 250 frequencies in random order, averaging for 50–250 microwave modulation periods. While the microwave lock-in improves the signal-to-noise ratio (SNR) at a given frequency sample, the intensity drift can still limit the measurement, as frequency switching is relatively slow: a fluctuation in laser power between two frequency samples causes fluctuations in relative contrast between the two samples. Our relatively inexpensive laser also exhibits random telegraph noise at times, and so some measurements are averaged up to five times to help alleviate this effect. The exact conditions in each measurement presented in the main figures are as follows: data in Figs. 1 and 2 are averaged for 100 microwave modulation periods per frequency sample, averaged once overall (approximately 20 min per measurement); unpolarized and unblocked data in Fig. 3 are averaged for 50 modulation periods per frequency sample, five times overall (approximately 75 min per measurement), while polarized and blocked data are averaged for 125 modulation periods per frequency sample, four times overall (approximately 155 min per measurement for each of the four polarization and beam block combinations); unpolarized and unblocked data in Fig. 4 are averaged for 100 modulation periods per frequency sample, averaged once overall (approximately 35 min per measurement), while polarized and blocked data of Fig. 4 are averaged for 250 modulation periods per frequency sample, averaged once overall (approximately 85 min per measurement for each of the four polarization and beam block combinations). A significant amount of dead time is included in each of the measurement durations reported above, due largely to lags in communication with the microwave synthesizer and online data transfer between LabView and MATLAB after each frequency step. We can afford to work well below optimum efficiency here since our samples are static and contain relatively strong magnetic features. This inefficiency can certainly be improved for more demanding measurements.

Before each measurement, diamond chips are cleaned by sonicating for 30 min in acetone, then 30 min in isopropyl alcohol. Ferromagnetic 2-μm-diameter bead (Spherotech) samples are prepared by diluting 1/100 from stock, sonicating for 30 min, then pipetting an aliquot onto the NV-layer surface of the diamond chip and leaving to dry on top of a permanent magnet in order to preferentially orient the beads at the surface.

Paleomagnetism measurements are done by placing the rock surface in contact with the NV-layer surface of the diamond. Before magnetic imaging, we apply a 2000-G IRM [31] field to the Allende sample. This step allows us to more easily identify magnetic sources for this proof of principle and to simulate a highly magnetized meteorite sample in order to illustrate the dynamic range-extending capability of Fourier decomposition imaging over conventional vector imaging.

APPENDIX C: ANALYSIS

For both Fourier-space and real-space measurements, ODMR image data are stored as three-dimensional (two spatial and one microwave frequency) arrays to be analyzed with custom MATLAB software. To analyze Fourier-space images such as those in Fig. 1 and Fig. S7 of Ref. [24], each 237×237 pixel image is first smoothed with a Gaussian filter ($\sigma = 5$ pixels). A slight 4° rotation of the images due to subtle misalignments in the reflection axes of our mirrors is corrected in postprocessing for analysis of the Fourier plane. We compute the elements of the transformation matrix $\mathbf{W}$ from these images. As we mention in the main text, in practice, we do not enforce the symmetry of Eq. (3) and instead use the experimentally measured matrix elements. For sample $D1$ measured with the 1.49/oil objective, the experimentally measured matrix is

$$\mathbf{W} = \begin{pmatrix} 0.222 & 0.355 & 0.058 & 0.358 \\ 0.351 & 0.213 & 0.354 & 0.060 \\ 0.062 & 0.371 & 0.222 & 0.359 \\ 0.365 & 0.060 & 0.367 & 0.222 \end{pmatrix}. \quad \text{(C1)}$$

The matrix entries are similar to the simulated values quoted in the main text. The simulations dictate that we

should expect a different $\mathbf{W}$ when detecting NVs through the diamond using the NA 0.75 air-immersion objective. In this case, we find simulated values of $w_1 = 0.175$, $w_2 = 0.370$, and $w_3 = 0.085$. Again, in practice, we use the experimentally measured transformation matrix, now given by

$$\mathbf{W} = \begin{pmatrix} 0.178 & 0.366 & 0.090 & 0.374 \\ 0.363 & 0.172 & 0.364 & 0.085 \\ 0.094 & 0.368 & 0.176 & 0.375 \\ 0.366 & 0.094 & 0.370 & 0.166 \end{pmatrix}. \quad \text{(C2)}$$

The above is used for lower-NA measurements of sample $D1$. The values change very slightly for the thinner NV layer of sample $D2$.

For real-space measurements, the aforementioned 4° rotation is compensated by a commensurate rotation of the polarizer axis and knife edge away from horizontal or vertical. Rotating the polarizer and beam block between each $\tilde{c}_i(x_k, y_k f)$ measurement causes small but measurable relative shifts of the images. To coregister the real-space images with one another, we compute their cross-correlations then shift to compensate the offset between the peaks of the correlation functions before further analysis. Blocking half of the pupil results in an elongated PSF (see Fig. S2 in Ref. [24]), which, in turn, means that the image of a point source recorded with the left or right half of the pupil blocked will not completely overlap with an image of the same point source recorded with the top or bottom of the pupil blocked. To compensate for this incomplete overlap, we perform Lucy-Richardson deconvolution on each slice of the ODMR image using the simulated PSF (again rotated by 4°) (see Fig. S2 in Ref. [24]) and the MATLAB function `deconvlucy`. While this deconvolution step appears to improve magnetic bead images as determined by visual comparison to high-field images, it does not noticeably affect the images of the rock's magnetic features, and so it is not included in the analysis of the data presented in Fig. 4. The difference is likely explained by the fact that the magnetic features due to the rock are higher in magnitude and spatially broader than those of the beads. The deconvolution step is likely to be more important for small signals and spatial resolutions approaching the diffraction limit. In analyzing the unpolarized and unblocked data presented in Figs. 3(b)–3(d), we include a deconvolution step using the appropriate unblocked simulated PSF (see Fig. S2 in Ref. [24]) for the sake of fair comparison.

We find that data taken with the Fourier decomposition method are somewhat sensitive to the objective's focal position. As shown in Fig. S2 of Ref. [24], the focal plane is ill-defined when imaging through the bulk diamond due to the appearance of sidelobes along the optical axis. The central spot of the simulated lateral PSF is, in fact, narrower when the objective is positioned at the second-brightest peak along z. Experimentally, we also note something resembling multiple foci and seem to find best results when positioned at the second-deepest such focal point. For deconvolution, we use the lateral slice of the PSF corresponding to the simulated second focal position (see Fig. S2 in Ref. [24]).

Since the features imaged in our studies do not necessitate such fine pixelation to resolve, we low-pass filter the data by applying a Gaussian blur ($\sigma = 20$ pixels) and then binning (10×10 for magnetic bead imaging, 25×25 for rock imaging) the image at each frequency slice. The strong, localized magnetic features of the Allende section imbue steep magnetic field gradients on the NVs, causing significant broadening of the resonances. These broadened spectra are smoothed via a boxcar average of length 5 applied along the frequency axis before fitting. No such frequency boxcar is applied to the magnetic bead data.

The spectrum in each pixel is fit with specified line shapes using least-squares fitting. For each NV orientation, we fit each resonance line shape as the sum of three Lorentzian functions separated by 2.16 MHz to account for ^{14}N hyperfine splitting. The width, height, and central frequency of the Lorentzians are free parameters of the fit. Thus, for each NV orientation, this yields a total of either four (one height, one width, and two positions) or six (two heights, two widths, and two positions) free parameters—the difference between the two cases is insignificant. Once the positions of each of the $2 \times 4 = 8$ resonances are extracted, they are fed to a least-squares fit of the Hamiltonian with parameters B_x, B_y, B_z, M_{1z}, M_{2z}, M_{3z}, and M_{4z} (see Appendix D). An additional Gaussian blur is then applied to the resulting magnetic images ($\sigma = 0.5$ pixels for magnetic bead imaging, $\sigma = 1$ pixel for rock imaging).

The slowly varying applied bias magnetic field is removed from images of magnetic beads by fitting the entire image (field of view approximately $150 \times 150\,\mu\text{m}^2$) to a fourth-order polynomial and subtracting the offset. The images of the magnetic bead shown in Fig. 3 are only a small subset of the mostly empty images recorded around it. A different approach to background subtraction is used for the rock sample since slowly varying recorded magnetic fields may be the result of real sources buried deeper within the rock. In this case, we measure the background magnetic image due solely to the bias field by removing the rock slice from the diamond and then subtract this resulting map from the rock magnetic images.

Finally, magnetic bead images are fit with least squares to a magnetic dipole source image with six free parameters: x position, y position, standoff distance, magnetic dipole moment, azimuthal orientation, and polar orientation. The rock image shown in Fig. 4 is fit to two such dipole sources plus a linearly varying background (see Fig. S6 in Ref. [24]).

APPENDIX D: HAMILTONIAN MODEL

The relevant spin Hamiltonian (in frequency units) for the NV oriented parallel to $\hat{\mathbf{u}}_1$ is

$$\mathscr{H}_1 = (D + M_{z1})\left(S_{z1}^2 - \frac{2}{3}\right) + \gamma \mathbf{S}_1 \cdot \mathbf{B} - M_{x1}(S_{x1}^2 - S_{y1}^2) + M_{y1}(S_{x1}S_{y1} + S_{y1}S_{x1}) + \mathbf{S}_1 \cdot \mathbf{A} \cdot \mathbf{I}. \quad \text{(D1)}$$

In Eq. (D1), $D = 2.87$ GHz is the zero-field splitting, $\mathbf{S}_1$ is the electronic spin operator, $\gamma = 2.8$ MHz/G is the electronic gyromagnetic ratio, $\mathbf{B}$ is the magnetic field, terms including components of $\mathbf{M}_1$ account for the spin-stress interaction [35,36] (see below), $\mathbf{I}$ is the ^{14}N nuclear spin operator, and $\mathbf{A}$ is the associated hyperfine tensor. The coordinate system $\{x_1, y_1, z_1\}$ is defined such that z_1 points along $\hat{\mathbf{u}}_1$, and x_1 coincides with one of the mirror planes of a NV with this orientation. Analogous Hamiltonians are defined for the other three NV orientations, with $\{x_j, y_j, z_j\} \forall j \in \{1, 2, 3, 4\}$ related to one another and to the lab frame coordinates $\{x, y, z\}$ referred to in Fig. 1 via the appropriate rotation matrices.

The components of $\mathbf{M}_1$ are related to the stress tensor $\bar{\bar{\sigma}}$ as described in Refs. [35,36] and to those of $\mathbf{M}_j$ for $j \neq 1$ via rotation matrix transformations of $\bar{\bar{\sigma}}$. In fitting, we neglect terms proportional to M_{x_j} and M_{y_j} yielding the simplified Hamiltonian:

$$\mathscr{H}_j = (D + M_{z_j})\left(S_{z_j}^2 - \frac{2}{3}\right) + \gamma \mathbf{S}_j \cdot \mathbf{B} + \mathbf{S}_j \cdot \mathbf{A} \cdot \mathbf{I} \quad \text{(D2)}$$

for each j. This approximation is justified by considering a magnetic field oriented along $\hat{\mathbf{u}}_j$ and treating $\mathbf{M}_j$ perturbatively. For the $0 \rightarrow +1$ transition, to second order:

$$f_{0\rightarrow+1} = D + \gamma B_{z_j} + M_{z_j} + \frac{M_{x_j}^2 + M_{y_j}^2}{2\gamma B_{z_j}}. \quad \text{(D3)}$$

For our work, we expect only modest amounts of stress due to lattice imperfections, with $M_{x_j} \approx M_{y_j} \approx M_{z_j} \approx$ 0.1 MHz. In this case, again considering the fact that the minimum Zeeman splitting due to the applied field is approximately 4 MHz in our studies, the third term on the rhs in Eq. (D3) contributes a correction of approximately 0.1 MHz, while the fourth term contributes only a correction of approximately 2.5 kHz. A future application at $|\mathbf{B}^{(\text{bias})}| < \sim 1$ G may necessitate measuring each $\{M_{x_j}, M_{y_j}, M_{z_j}\}$ associated with the diamond region first without the sample.

[1] R. Schirhagl, K. Chang, M. Loretz, and C. L. Degen, Nitrogen-vacancy centers in diamond: Nanoscale sensors for physics and biology, Annu. Rev. Phys. Chem. **65**, 83 (2014).

[2] L. Rondin, J. P. Tetienne, T. Hingant, J. F. Roch, P. Maletinsky, and V. Jacques, Magnetometry with nitrogen-vacancy defects in diamond, Rep. Prog. Phys. **77**, 056503 (2014).

[3] J. M. Taylor, P. Cappellaro, L. Childress, L. Jiang, D. Budker, P. R. Hemmer, A. Yacoby, R. Walsworth, and M. D. Lukin, High-sensitivity diamond magnetometer with nanoscale resolution, Nat. Phys. **4**, 810 (2008).

[4] J. Tetienne, N. Dontschuk, D. A. Broadway, A. Stacey, D. A. Simpson, and L. C. Hollenberg, Quantum imaging of current flow in graphene, Sci. Adv. **3**, e1602429 (2017).

[5] D. R. Glenn, K. Lee, H. Park, R. Weissleder, A. Yacoby, M. D. Lukin, H. Lee, R. L. Walsworth, and C. B. Connolly, Single-cell magnetic imaging using a quantum diamond microscope, Nat. Methods **12**, 736 (2015).

[6] D. Le Sage, K. Arai, D. R. Glenn, S. J. DeVience, L. M. Pham, L. Rahn-Lee, M. D. Lukin, A. Yacoby, A. Komeili, and R. L. Walsworth, Optical magnetic imaging of living cells, Nature (London) **496**, 486 (2013).

[7] R. R. Fu, B. P. Weiss, E. A. Lima, P. Kehayias, J. F. Araujo, D. R. Glenn, J. Gelb, J. F. Einsle, A. M. Bauer, R. J. Harrison, G. A. H. Ali, and R. L. Walsworth, Evaluating the paleomagnetic potential of single zircon crystals using the Bishop Tuff, Earth Planet. Sci. Lett. **458**, 1 (2017).

[8] R. R. Fu, B. P. Weiss, E. A. Lima, R. J. Harrison, X. Bai, S. J. Desch, D. S. Ebel, C. Suavet, H. Wang, D. Glenn, D. Le Sage, T. Kasama, R. L. Walsworth, and A. T. Kuan, Solar nebula magnetic fields recorded in the Semarkona meteorite, Science **346**, 1089 (2014).

[9] M. W. Doherty, F. Dolde, H. Fedder, F. Jelezko, J. Wrachtrup, N. B. Manson, and L. Hollenberg, Theory of the ground-state spin of the NV–center in diamond, Phys. Rev. B **85**, 205203 (2012).

[10] D. R. Glenn, R. R. Fu, P. Kehayias, D. Le Sage, E. A. Lima, B. P. Weiss, and R. L. Walsworth, Micrometer-scale magnetic imaging of geological samples using a quantum diamond microscope, Geochem. Geophys. Geosys. **18**, 3254 (2017).

[11] F. Etoc, D. Lisse, Y. Bellaiche, J. Piehler, M. Coppey, and M. Dahan, Subcellular control of Rac-GTPase signalling by magnetogenetic manipulation inside living cells, Nat. Nanotechnol. **8**, 193 (2013).

[12] B. A. Kalinikos and A. N. Slavin, Theory of dipole-exchange spin wave spectrum for ferromagnetic films with mixed exchange boundary conditions, J. Phys. C **19**, 7013 (1986).

[13] I. Źutić, J. Fabian, and S. D. Sarma, Spintronics: Fundamentals and applications, Rev. Mod. Phys. **76**, 323 (2004).

[14] J. W. Goodman, *Introduction to Fourier Optics* (Roberts and Company Publishers, Greenwood Village, CO, 2005).

[15] M. Lesik, J. Tetienne, A. Tallaire, J. Achard, V. Mille, A. Gicquel, J. Roch, and V. Jacques, Perfect preferential orientation of nitrogen-vacancy defects in a synthetic diamond sample, Appl. Phys. Lett. **104**, 113107 (2014).

[16] V. M. Acosta, A. Jarmola, E. Bauch, and D. Budker, Optical properties of the nitrogen-vacancy singlet levels in diamond, Phys. Rev. B **82**, 201202 (2010).

[17] R. J. Epstein, F. M. Mendoza, Y. K. Kato, and D. D. Awschalom, Anisotropic interactions of a single spin and dark-spin spectroscopy in diamond, Nat. Phys. **1**, 94 (2005).

[18] A. S. Backer and W. E. Moerner, Extending single-molecule microscopy using optical Fourier processing, J. Phys. Chem. B **118**, 8313 (2014).
[19] L. Novotny and B. Hecht, *Principles of Nano-Optics* (Cambridge University Press, Cambridge, England, 2012).
[20] B. Richards and E. Wolf, Electromagnetic diffraction in optical systems, II. Structure of the image field in an aplanatic system, Proc. R. Soc. A **253** (1959).
[21] M. Böhmer and J. Enderlein, Orientation imaging of single molecules by wide-field epifluorescence microscopy, J. Opt. Soc. Am. B **20**, 554 (2003).
[22] M. A. Lieb, J. M. Zavislan, and L. Novotny, Single-molecule orientations determined by direct emission pattern imaging, J. Opt. Soc. Am. B **21**, 1210 (2004).
[23] D. Axelrod, Fluorescence excitation and imaging of single molecules near dielectric-coated and bare surfaces: A theoretical study, J. Microsc. **247**, 147 (2012).
[24] See the Supplemental Material at http://link.aps.org/supplemental/10.1103/PhysRevApplied.8.054003 for notes on sensitivity comparison and additional figures.
[25] J. Herrmann, M. A. Appleton, K. Sasaki, Y. Monnai, T. Teraji, K. M. Itoh, and E. Abe, Polarization-and frequency-tunable microwave circuit for selective excitation of nitrogen-vacancy spins in diamond, Appl. Phys. Lett. **109**, 183111 (2016).
[26] M. Mrózek, J. Mlynarczyk, D. S. Rudnicki, and W. Gawlik, Circularly polarized microwaves for magnetic resonance study in the GHz range: Application to nitrogen-vacancy in diamonds, Appl. Phys. Lett. **107**, 013505 (2015).
[27] T. P. M. Alegre, C. Santori, G. Medeiros-Ribeiro, and R. G. Beausoleil, Polarization-selective excitation of nitrogen vacancy centers in diamond, Phys. Rev. B **76**, 165205 (2007).
[28] C. P. Hunt, M. J. Singer, G. Kletetschka, J. TenPas, and K. L. Verosub, Effect of citrate-bicarbonate-dithionite treatment on fine-grained magnetite and maghemite, Earth Planet. Sci. Lett. **130**, 87 (1995).
[29] P. J. Davis, *Circulant Matrices* (American Mathematical Society, Providence, 2012).
[30] R. R. Fu, E. A. Lima, and B. P. Weiss, No nebular magnetization in the Allende CV carbonaceous chondrite, Earth Planet. Sci. Lett. **404**, 54 (2014).
[31] L. Tauxe, *Paleomagnetic Principles and Practice* (Kluwer, Dordrecht, 1998).
[32] M. P. Backlund, A. Arbabi, P. N. Petrov, E. Arbabi, S. Saurabh, A. Faraon, and W. E. Moerner, Removing orientation-induced localization biases in single-molecule microscopy using a broadband metasurface mask, Nat. Photonics **10**, 459 (2016).
[33] G. Popescu, T. Ikeda, R. R. Dasari, and M. S. Feld, Diffraction phase microscopy for quantifying cell structure and dynamics, Opt. Lett. **31**, 775 (2006).
[34] F. Münzhuber, J. Kleinlein, T. Kiessling, and L. W. Molenkamp, Polarization-assisted vector magnetometry in zero bias field with an ensemble of nitrogen-vacancy centers in diamond, arXiv:1701.01089.
[35] M. S. Barson, P. Peddibhotla, P. Ovartchaiyapong, K. Ganesan, R. L. Taylor, M. Gebert, Z. Mielens, B. Koslowski, D. A. Simpson, and L. P. McGuinness, Nanomechanical sensing using spins in diamond, Nano Lett. **17**, 1496 (2017).
[36] F. Grazioso, B. R. Patton, P. Delaney, M. L. Markham, D. J. Twitchen, and J. M. Smith, Measurement of the full stress tensor in a crystal using photoluminescence from point defects: The example of nitrogen vacancy centers in diamond, Appl. Phys. Lett. **103**, 101905 (2013).